

SLICT: Multi-input Multi-scale Surfel-Based Lidar-Inertial Continuous-Time Odometry and Mapping

Thien-Minh Nguyen^{1*}, Daniel Duberg¹, Patric Jensfelt¹,
Shenghai Yuan², Lihua Xie², *Fellow, IEEE*

Abstract—While feature association to a *global map* has significant benefits, to keep the computations from growing exponentially, most lidar-based odometry and mapping methods opt to associate features with *local maps* at one voxel scale. Taking advantage of the fact that *surfels* (surface elements) at different voxel scales can be organized in a tree-like structure, we propose an octree-based global map of *multi-scale* surfels that can be updated incrementally. This alleviates the need for recalculating, for example, a k-d tree of the whole map repeatedly. The system can also take input from a single or a number of sensors, reinforcing the robustness in degenerate cases. We also propose a point-to-surfel (PTS) association scheme, continuous-time optimization on PTS and IMU preintegration factors, along with loop closure and bundle adjustment, making a complete framework for Lidar-Inertial continuous-time odometry and mapping. Experiments on public and in-house datasets demonstrate the advantages of our system compared to other state-of-the-art methods. To benefit the community, we release the source code and dataset at <https://github.com/brytsknguyen/slict>.

I. INTRODUCTION

Thanks to reduced cost and weight, lidar-based navigation systems have made many significant progresses for autonomous systems in recent years, motivating many new advanced algorithms. In this paper, we are concerned with two main aspects of a lidar-inertial odometry and mapping (LIOM) system, namely feature extraction-association, and mapping.

For feature extraction-association (also termed the *front-end* [1]), existing methods can be grouped into three main categories. In the first one, planar and corner features are extracted based on the smoothness value, then associated with k-nearest neighbours to construct the corresponding cost factors. This method was proposed in [2] and is still widely adopted in many recent works [3]–[7]. One issue of this method is that the smoothness calculation is specialized for the lidar scans with horizontally separated rings, in environments with man-made structure. To overcome this issue, in FAST-LIO [8], [9], Xu et al propose the *direct method*, where each lidar point is directly associated with

¹ Division of Robotics, Perception and Learning, KTH Royal Institute of Technology, Stockholm, 11428, (e-mail: tmng@kth.se, dduberg@kth.se, patric@kth.se).

² School of Electrical and Electronic Engineering, Nanyang Technological University, Singapore 639798, 50 Nanyang Avenue. (e-mail: shyuan@ntu.edu.sg, elhxie@ntu.edu.sg)

This work was partially supported by the *Wallenberg AI, Autonomous Systems and Software Program (WASP)*, funded by the Knut and Alice Wallenberg Foundation, under the Wallenberg-NTU Presidential Postdoctoral Fellowship Program.

* Corresponding author.

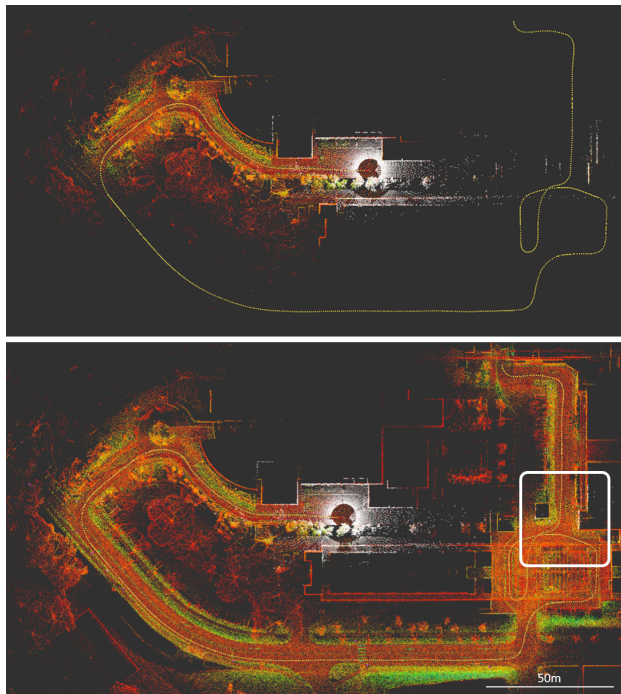


Fig. 1: While a local map (top) helps keep computation bounded, it limits the association only to recent marginalized features, which gives chance to estimation drift relative to the initial state. In contrast, with a global map, we can achieve early association with the earliest features (white box) and reinforce global consistency.

a neighborhood in the map. The method can work well with both the common spinning lidars (Ouster/Velodyne) and prism-based box-shaped lidar (Livox). We find that direct method combined with the filter-based update scheme achieves quite good result ([8]–[11]) for a smaller computation footprint compared to more computationally demanding iterative gradient-based optimization.

In another approach, high-abstraction features such as planes, lines [12], [13] can be extracted and treated as landmarks. The landmarks' coefficients will also be jointly estimated with the robot states, in similar fashion with visual-inertial odometry (VIO) systems. This approach has the benefit of dealing with a smaller amount of features. However, the feature extraction process is more complex and may not be able to detect planes or lines in cluttered or unstructured environments such as forests or mines.

In this work, we propose the use of surfel-based features

at different resolutions for the frontend task. Different from geometric features such as planes or edges, surfels are characterized by ellipsoidal fitting parameters [14], with complexity between that of the direct method and high-abstraction features. Moreover, surfels can be detected and associated at different scales, which allow us to add more factors in the graph optimization to reinforce the registration of lidar scans with large scale surfaces in the map. Instead of associating surfel to surfel like previous works [14]–[16], which requires complicated processes that involve surfelizing the input scans, then associating up-to-scale surfels using k-NN search based on high dimensional descriptors, and rejecting some associations based on timestamps and velocities [15], we propose a simpler strategy that directly matches the lidar points to surfels at all possible scales, as long as a high fitting score is met (Sec. III-D).

On the mapping side, the update and query processes require special attention. In most conventional systems, a k-d tree structure is built to accelerate the k-NN querying process. However, as the map grows, recomputing the k-d tree on the global map is intractable. One strategy to avoid this issue is to organize the maps into keyframes and build a local map with bounded size from a finite number of nearest keyframes [3]–[5], [7], [14]. However this strategy is sub-optimal since there are cases where the local map misses important prior observations that were captured in previous keyframes (an example is given in Fig. 1). To maintain efficient queries on a single global map, in [9], Xu et al proposes the ikd-Tree framework, which allows one to incrementally update the k-d tree of the map without having to recompute all distances from scratch. So far, the ikd-Tree only manages point-based incrementally updated map. In this paper, we propose a more generalized incremental tree of surfels, based on the UFOMap framework [17].

The contributions in our work can be listed as follows:

- A full-fledged Lidar-Inertial Odometry and Mapping framework with frontend odometry, loop closure and global pose-graph optimization, capable of integrating multiple lidar inputs.
- A multi-scale point-to-surfel (PTS) association strategy and continuous-time optimization of PTS and IMU preintegration factors on a sliding window.
- An implementation of a hierarchical multi-scale surfel map based on the UFOMap framework, enabling incremental update and efficient query of the global map.
- Extensive experiments on public and in-house datasets to validate the results and effects of the multi-scale surfel association strategy.
- We release the source code and the datasets for the benefit of the community.

Henceforth, we refer to our method as SLICT (*Surfel-based Lidar-Inertial Continuous-Time Odometry and Mapping*) for short. The remaining of the paper is as follows: Sec. II provides some preliminary definitions for our problems, where Sec. II-D details the surfel tree and its implementation on the UFOMap. Sec. III describes in details the operation

of the main blocks in our system. Sec. IV describes our experiments on public and in-house datasets. Sec. V concludes our work and provides comments for future extension.

II. PRELIMINARY

A. Notation

In this paper for a vector $\mathbf{p} \in \mathbb{R}^3$, \mathbf{p}^\top denotes its transpose, and $[\mathbf{p}]_\times$ denotes the skew-symmetric matrix of \mathbf{p} . For a physical quantity \mathbf{p} , we use the hat notation $\hat{\mathbf{p}}$ to denote the optimization-based estimate of \mathbf{p} . Similarly, the breve notation $\breve{\mathbf{p}}$ is used to refer to an IMU-propogated estimate of \mathbf{p} . To avoid convoluting definitions, we may refer to $\hat{\mathbf{p}}$, $\breve{\mathbf{p}}$ without first formally defining \mathbf{p} .

The robot orientation can be represented by the rotation matrix, denoted as \mathbf{R} , or quaternion \mathbf{q} . The two representations can be used interchangeably as the conversion between them is well defined.

We reserve the left superscript for the coordinate frames of a quantity. For example, ${}^{B_{t_s}}\mathbf{f}$ denotes a vector \mathbf{f} whose coordinates are referenced in the robot’s body at time t_s . For convenience we may also write ${}^{B_{t_s}}\mathbf{f}$ as ${}^{t_s}\mathbf{f}$.

B. State estimate

We define a sliding window spanning a time interval $[t_w, t_k]$, with M time instances (t_w, t_k included). Each t_m is associated with a state estimate $\hat{\mathcal{X}}_m$ defined as follows:

$$\hat{\mathcal{X}}_m = (\hat{\mathbf{R}}_m, \hat{\mathbf{p}}_m, \hat{\mathbf{v}}_m, \hat{\mathbf{b}}_{gm}, \hat{\mathbf{b}}_{am}) \in \text{SO}(3) \times \mathbb{R}^{12}, \quad (1)$$

where $\hat{\mathbf{R}}_m \in \text{SO}(3)$, $\hat{\mathbf{p}}_m, \hat{\mathbf{v}}_m \in \mathbb{R}^3$ are respectively the state estimates of the rotation matrix, position and velocity of the robot, and $\hat{\mathbf{b}}_{gm} \in \mathbb{R}^3, \hat{\mathbf{b}}_{am} \in \mathbb{R}^3$ are the IMU gyroscope and accelerometer biases.

C. Maximum-A-Priori (MAP) Optimization

The core of our system lies in solving the following MAP optimization problem:

$$f(\hat{\mathcal{X}}) = \sum_{m=w}^{k-1} \left\| r_{\mathcal{I}}(\mathcal{I}_m, \hat{\mathcal{X}}_m, \hat{\mathcal{X}}_{m+1}) \right\|_{\Sigma_{\mathcal{I}}}^2 + \sum_{m=w}^{k-1} \sum_{\mathcal{L} \in \mathcal{A}_m} \left\| r_{\mathcal{L}}(\mathcal{L}({}^{B_{t_s}}\mathbf{f}, \mathbf{n}, \mu, s), \hat{\mathcal{X}}_m, \hat{\mathcal{X}}_{m+1}) \right\|_{\Sigma_{\mathcal{L}}}^2, \quad (2)$$

where:

- $r_{\mathcal{I}}$ is the cost factor of the preintegration \mathcal{I}_m , which is constructed from the IMU samples in the interval $[t_m, t_{m+1}]$, and $\Sigma_{\mathcal{I}}$ is the corresponding covariance matrix;
- $r_{\mathcal{L}}$ denotes a lidar PTS factor based on a tuple of PTS association coefficients $\mathcal{L}({}^{B_{t_s}}\mathbf{f}, \mathbf{n}, \mu, s)$, and $\Sigma_{\mathcal{L}}$, a covariance, which is scalar in this case;
- \mathbf{n}, μ are the normal and mean of the underlying associated surfel (Sec. II-D.1), and $s = \frac{t_s - t_m}{t_{m+1} - t_m}$ is the normalized time stamp of raw lidar point ${}^{B_{t_s}}\mathbf{f}$ (elaborated in III-D).
- Finally \mathcal{A}_m denotes the set of successful PTS associations in $[t_m, t_{m+1}]$ (more details are given in III-D).

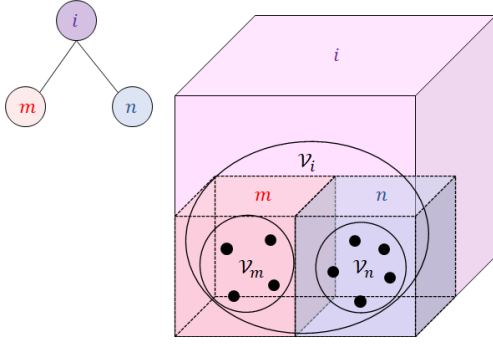


Fig. 2: Illustration of surfel and the tree-like structure: A voxel i contains a set of points \mathcal{V}_i , which (in this example) contains two subsets $\mathcal{V}_m, \mathcal{V}_n$, encapsulating the points in the voxels m, n at smaller scales. Each of the sets $\mathcal{V}_i, \mathcal{V}_m, \mathcal{V}_n$ define a surfel whose attributes are described in Section II-D.1. As $\mathcal{V}_m \subset \mathcal{V}_i, \mathcal{V}_n \subset \mathcal{V}_i$, there is a hierarchical relationship between the surfels, which we propose to organize in an octree implemented by the UFOMap framework.

It should be noted that each point $B_{t_s} \mathbf{f}$ can be associated with multiple surfels at different scales, as long as the surfel satisfies the association predicates in Sec. III-D.

We refer to our method as continuous-time LIOM based on the use of continuous-time factor $r_{\mathcal{L}}(\mathcal{L}(B_{t_s} \mathbf{f}), \hat{\mathcal{X}}_m, \hat{\mathcal{X}}_{m+1})$, which is based on raw lidar point $B_{t_s} \mathbf{f}$. This characterization is consistent with previous works [7], [14]. In contrast, discrete-time methods use the deskewed point $B_{t_s} \mathbf{f}$ based on IMU-propagated states [3], [4], [18]. To couple $B_{t_s} \mathbf{f}$ with the states $\hat{\mathcal{X}}_m, \hat{\mathcal{X}}_{m+1}$, we use a linear interpolation formulation based on the time stamp t_s of $B_{t_s} \mathbf{f}$, which is elaborated in Sec. III-D.

D. Surfel and UFOMap

1) *Surfel's attributes*: A node i in the octree-based UFOMap corresponds to a voxel, and the node's depth indicates the voxel's scale. For leaf nodes, they are assigned depth 0, its parent has depth 1, and so forth. A surfel at node i in the UFOMap is defined by the set of points contained within the voxel, denoted as $\mathcal{V}_i = \{\mathbf{f}_1, \dots, \mathbf{f}_{N_i}\}$. The following quantities make up the basic attributes of the surfel:

$$N_i = |\mathcal{V}_i|, \mathbf{S}_i \triangleq \sum_{k=1}^{N_i} \mathbf{f}_k, \mathbf{C}_i \triangleq \sum_{k=1}^{N_i} \mathbf{f}_k \mathbf{f}_k^\top - \frac{1}{N_i} \mathbf{S}_i \mathbf{S}_i^\top. \quad (3)$$

Each surfel in UFOMap stores the values $N_i, \mathbf{S}_i, \mathbf{C}_i$. Given these attributes, we can quickly compute the mean μ_i and covariance Γ_i of \mathcal{V}_i , along with other quantities as follows:

$$\mu_i \triangleq \frac{1}{N_i} \mathbf{S}_i, \Gamma_i \triangleq \frac{1}{N_i - 1} \mathbf{C}_i, \lambda_0 \leq \lambda_1 \leq \lambda_2, \\ \rho_i = 2 \frac{\lambda_1 - \lambda_0}{\lambda_0 + \lambda_1 + \lambda_2}, \mathbf{n}_i \triangleq \nu_0, c_i \triangleq -\nu_0^\top \mu_i.$$

where μ_i is the mean, Γ_i is the covariance with the eigenvalues $\lambda_0, \lambda_1, \lambda_2$ and $\mathbf{n}_i = \nu_0$ is the normalized eigenvector associated with λ_0 ; ρ_i is the so-called *planarity* value, i.e. the plane-likeness metric of the surfel.

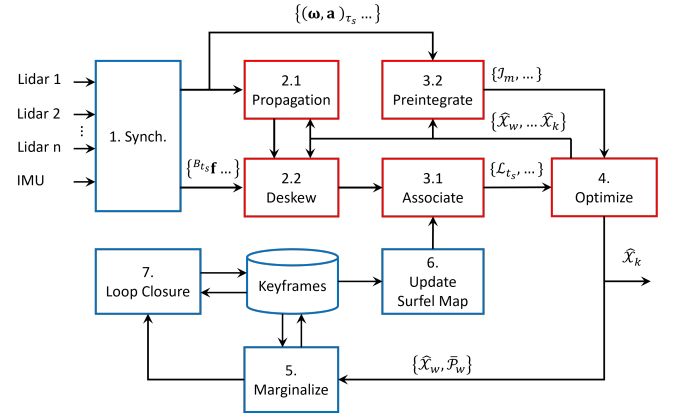


Fig. 3: The general workflow of the system. More details are given in Sec. III-A - Sec. III-I

Besides the aforementioned attributes, the *depth* and *scale* of the voxel node are also frequently queried. To initialize a surfel map in the UFOMap framework, we assign a *leaf node size*, denoted ℓ , for the voxels at the smallest scale, i.e., at depth 0. The scale of a voxel at depth D is therefore $2^D \ell$.

2) *Surfel addition and subtraction*: Assuming that a parent node i has two children m and n , the surfel attributes of i can be calculated via Welford's formula [19]:

$$\alpha := 1 / [N_m N_n (N_m + N_n)], \beta := N_n \mathbf{S}_m - N_m \mathbf{S}_n, \\ \mathbf{C}_i \leftarrow \mathbf{C}_m + \mathbf{C}_n + \alpha \beta \beta^\top, \\ N_i \leftarrow N_m + N_n, \mathbf{S}_i \leftarrow \mathbf{S}_m + \mathbf{S}_n, \quad (4)$$

The above can be iterated for parent nodes with more than two children.

Based on (4), if the child node n is removed from the map, the surfel attributes of i can be updated by the procedure:

$$N_i \leftarrow N_i - N_n, \mathbf{S}_i \leftarrow \mathbf{S}_i - \mathbf{S}_n, \\ \alpha := 1 / [N_i N_n (N_i + N_n)], \beta := N_n \mathbf{S}_i - N_i \mathbf{S}_n, \\ \mathbf{C}_i \leftarrow \mathbf{C}_i - \mathbf{C}_n - \alpha \beta \beta^\top. \quad (5)$$

For single point update, i.e. the update at the leaf nodes when new pointcloud is added to the UFOMap, we can still use (4), (5) by noticing that when $N_n = 1, \mathbf{C}_n = 0$.

III. SYSTEM DESCRIPTION

Fig. 3 provides an overview of our system. In the next subsections we describe in details each numbered block.

A. Synchronization

Synchronization is a prerequisite to optimization based estimation methods. Fig. 4 gives a brief explanation of our synchronization scheme. More details are given below.

The sliding window's progression is based on the arrival time of new lidar messages from a so-called *primary* lidar. The messages from each lidar are stored in an ordered buffer such that data from each lidar can be treated as a continuous stream. As the window shifts from $[t_w - \Delta_l, t_k - \Delta_l]$ to $[t_w, t_k]$, (where Δ_l is the sweeping period of the primary lidar, typically 0.1s), we extract data points from all the lidar

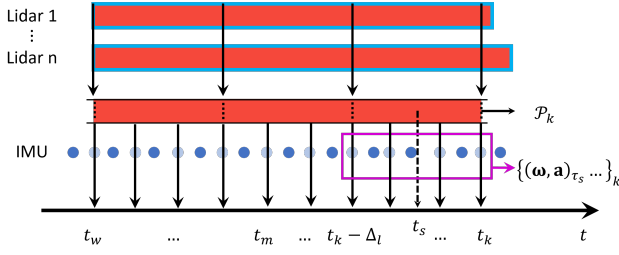


Fig. 4: Synchronization scheme on the sliding window: the window is shifted forward by Δ_l seconds based on the arrival time of the primary lidar messages. Data from each lidar is treated as a continuous stream of points. At time t_k , we extract and merge all points that fall in the period $[t_k - \Delta_l, t_k]$ into a single pointcloud \mathcal{P}_k . Similarly, IMU samples during $[t_k - \Delta_l, t_k]$ are also extracted and associated with \mathcal{P}_k . On the sliding window, we define a number of time instances $t_m \in [t_w, t_k]$, each is associated with a state estimate $\hat{\mathcal{X}}_m$. For each lidar point, we use their time stamp t_s to find the interval $[t_m, t_{m+1}] \ni t_s$, and the same for IMU sample. The interval $[t_m, t_{m+1}]$ determines the state estimates $\hat{\mathcal{X}}_m, \hat{\mathcal{X}}_{m+1}$ that are coupled with the lidar or IMU measurements in (2).

streams in the period $[t_k - \Delta_l, t_k]$ and merge them into a unified pointcloud \mathcal{P}_k .

Similarly, IMU samples are also stored in a buffer, and when the window slides forward for Δ_l seconds, the IMU samples in the periods $[t_k - \Delta_l, t_k]$ are also extracted and put onto the sliding window.

When a new lidar pointcloud is admitted to the sliding window, we also add one or more state estimates to the sliding window. Thus the number of pointclouds can be smaller than the number of state estimates, which is different from our previous work MILIOM [4]. The addition of more than one state estimates per newly added pointcloud is to better capture the dynamics of the robot. In practice we add 2 to 8 new state estimates to the sliding window, depending on the frequency of the IMU.

B. IMU propagation

Given the IMU samples $\{(\boldsymbol{\omega}, \mathbf{a})_{\tau_i}, \dots\}$, $\tau_i \in [t_m, t_{m+1}]$, and the starting state $\hat{\mathcal{X}}_m := \check{\mathcal{X}}_m$, we can forward propagate the robot state to $\check{\mathcal{X}}_{m+1}$, or backward propagate from $\hat{\mathcal{X}}_{m+1}$ to $\check{\mathcal{X}}_m$. After this process we have a sequence of IMU-propagated states $\{\check{\mathcal{X}}_{\tau_i}, \dots\}$, $\tau_i \in [t_m, t_{m+1}]$. This sequence can be used to initialize the new state estimate added to the sliding window, or to remove the motion-induced distortion of the pointcloud. We explain this so-called *deskew* process in the next part.

C. Deskew (motion compensation)

For each lidar point ${}^{B_{t_s}}\mathbf{f}$, $t_s \in [t_m, t_{m+1}]$ we seek to transform its coordinate to the body frame at time t_{m+1} . To this end, we search for the two IMU-propagated poses closest to t_s , i.e. $\check{\mathbf{T}}_{\tau_a}, \check{\mathbf{T}}_{\tau_b}$, where $\tau_a \leq t_s \leq \tau_b$, and find the

linearly interpolated pose $\check{\mathbf{T}}_{t_s}$:

$$\check{\mathbf{T}}_{t_s} = \begin{bmatrix} \text{slerp}(\check{\mathbf{R}}_{\tau_a}, \check{\mathbf{R}}_{\tau_b}, s) & (1-s)\mathbf{p}_{\tau_a} + s\mathbf{p}_{\tau_b} \\ 0 & 1 \end{bmatrix}, \quad (6)$$

where $s \triangleq \frac{t_s - \tau_a}{\tau_b - \tau_a}$ and $\text{slerp}()$ denotes the spherical linear interpolation operation on $\text{SO}(3)$.

Given $\check{\mathbf{T}}_{t_s}$, we can transform ${}^{B_{t_s}}\mathbf{f}$ to the world frame by $\mathbf{f} = \check{\mathbf{R}}_{t_s} {}^{B_{t_s}}\mathbf{f} + \hat{\mathbf{p}}_t s$. Hence we proceed to associating these lidar points with the surfel map.

D. Point-to-Surfel Association

The association consists of two stages. In the first stage, for each lidar point \mathbf{f} we find all the nodes \mathcal{V}_i matching the following predicates in the surfel map:

- The voxel depth is between 1 and D_{\max} (the leaf nodes are ignored).
- $N_i \geq N_{\min}$ and $\rho_i > \rho_{\min}$, i.e. \mathcal{V}_i should have at least N_{\min} points and the planarity is sufficiently large.
- The voxel's cube intersects with a sphere of radius $r > 0$ centered at \mathbf{f} , where r is a user-defined parameter.

If a surfel \mathcal{V}_i passes all of the aforementioned predicates, in the second stage we calculate the distance of \mathbf{f} to the underlying plane of \mathcal{V}_i , i.e. $d_i = \mathbf{n}_i^\top (\mathbf{f} - \boldsymbol{\mu}_i)$. If $d_i < d_{\max}$, a tuple of PTS coefficients $\mathcal{L} = ({}^{t_s}\mathbf{f}, \mathbf{n}_i, \mu_i, s)$, $s = \frac{t_s - t_m}{t_{m+1} - t_m}$ will be added to the set of successful association \mathcal{A}_m , which is then used to construct the cost function at the optimization stage (2).

Given \mathcal{L} , the cost factor $r_{\mathcal{L}}$ in (2) can be constructed as follows:

$$\begin{aligned} r_{\mathcal{L}} &= \mathbf{n}^\top (\hat{\mathbf{R}}_s {}^{t_s}\mathbf{f} + \hat{\mathbf{p}}_s - \boldsymbol{\mu}), \\ \hat{\mathbf{R}}_s &= \hat{\mathbf{R}}_m \text{Exp} \left[s \text{Log}(\hat{\mathbf{R}}_m^{-1} \hat{\mathbf{R}}_{m+1}) \right], \\ \hat{\mathbf{p}}_s &= (1-s)\hat{\mathbf{p}}_m + s\hat{\mathbf{p}}_{m+1}. \end{aligned} \quad (7)$$

E. IMU Preintegration

We refer to our previous work [4], [20] for the detailed formulation and Jacobian of IMU-preintegration factors in optimization-based estimation.

F. Optimization

Once all of the PTS coefficients and IMU preintegrations have been prepared, we proceed to construct and optimize the cost function (2) using the ceres solver [21]. It should be noted that the steps described in Sec. III-B to Sec. III-F (red boxes in Fig. 3) can be done iteratively.

G. Marginalization

After each optimization step, we check if the earliest pose estimate $\hat{\mathbf{T}}_w$ can be marginalized to become a keyframe. To this end, we search for five nearest neighbours of $\hat{\mathbf{T}}_w$ among the existing keyframes. If the Euclidean distance or rotational distance of $\hat{\mathbf{T}}_w$ to all of its neighbours exceeds a threshold, its associated deskewed pointcloud will be inserted to the surfel map. We also marginalize $\hat{\mathbf{T}}_w$ and store its deskewed pointcloud in the buffer to be reused in case of loop closure.

H. Updating the surfel map

When a new keyframe is admitted to the buffer, we also update the surfel map using the procedure that was introduced in Sec. II-D.2.

I. Loop Closure

When a new keyframe with the pose estimate $\hat{\mathbf{T}}_c$ is admitted to the buffer, we will find K nearest keyframes of $\hat{\mathbf{T}}_c$. If the time stamp of one keyframe $\hat{\mathbf{T}}_p$ and $\hat{\mathbf{T}}_m$ differs by a certain amount, it signals the return to a previously explored area. We use the ICP algorithm to calculate the relative pose ${}^p\bar{\mathbf{T}}_c$ between the two keyframes and store this in a buffer \mathcal{T} .

When a new loop is admit, we optimize the pose graph with this loop prior:

$$= \sum_{k=0}^{K-1} {}^k\bar{\mathbf{T}}_{k+1} \hat{\mathbf{T}}_k^{-1} \hat{\mathbf{T}}_{k+1} + \sum_{{}^p\bar{\mathbf{T}}_c \in \mathcal{T}} {}^p\bar{\mathbf{T}}_c \hat{\mathbf{T}}_p^{-1} \hat{\mathbf{T}}_c, \quad (8)$$

where ${}^k\bar{\mathbf{T}}_{k+1}$, ${}^p\bar{\mathbf{T}}_c$ are the relative pose priors, and \mathcal{T} is the set of relative poses detected. After the pose graph optimization, the global map will be recomputed.

IV. EXPERIMENTS

We demonstrate the performance of SLICT via three data suites: NTU VIRAL [22], Newer College [23] and our in-house datasets, which respectively capture operations at different scales.

We compare our methods with three other state-of-the-art methods. First is MARS [14], which stands for Multi-Adaptive-Resolution-Surfel with B-spline-based continuous-time optimization. Second is LIO-SAM [3], which uses conventional plane-edge feature and IMU preintegration factors, optimized by the Georgia Tech Smoothing and Mapping framework [24]. Third is FAST-LIO2, which uses the direct method for feature association and the ikd-Tree global mapping scheme.

A. NTU VIRAL Datasets

The NTU VIRAL is a multi-lidar dataset collected from an Unmanned Aerial Vehicles, with ground truth of centimeter-level accuracy obtained from a laser-tracker total station. The environments consist of indoor and outdoor spaces where the UAV operates within a volume of 50m radius.

For all experiments, we merge the data from the so-called horizontal and vertical lidars in the NTU VIRAL dataset and use them as the input of all four methods. All experiments are run on a core-i7 PC. The metric used in this case is the Absolute Trajectory Error (ATE).

In these experiments we do not enable the loop closure function of SLICT and only compare the odometry result. We set sensor’s parameters such as number of lines, minimum distance, IMU noises, etc, according to the dataset’s meta data, while other parameters are kept as default. For SLICT, we choose a sliding window of 400ms with 16 intervals, which encompass 4 pointclouds with 4 state estimates each.

TABLE I: ATE of SLICT compared with other methods on NTU VIRAL datasets (unit [m]). The best results are in **bold**, second best are underlined. ‘x’ denotes divergence.

| Dataset | MARS | LIO-SAM | FAST-LIO2 | SLICT |
|---------|---------|---------------|---------------|---------------|
| eee_01 | 0.2471 | 0.0624 | <u>0.0585</u> | 0.0316 |
| eee_02 | 0.1033 | 0.0457 | <u>0.0318</u> | 0.0249 |
| eee_03 | 0.0927 | 0.0403 | <u>0.0351</u> | 0.0275 |
| nya_01 | 0.0555 | 2.0960 | <u>0.0305</u> | 0.0229 |
| nya_02 | 0.0624 | x | <u>0.0286</u> | 0.0227 |
| nya_03 | 0.0831 | 0.0468 | <u>0.0315</u> | 0.0260 |
| sbs_01 | 0.1370 | 0.0444 | <u>0.0324</u> | 0.0298 |
| sbs_02 | 0.1256 | 0.0461 | <u>0.0322</u> | 0.0291 |
| sbs_03 | 0.1588 | 0.0494 | <u>0.0428</u> | 0.0335 |
| rtp_01 | x | 0.2571 | <u>0.0494</u> | 0.0447 |
| rtp_02 | 0.2329 | <u>0.1091</u> | 0.1151 | 0.0466 |
| rtp_03 | 0.1377 | 0.0576 | <u>0.0543</u> | 0.0501 |
| tnp_01 | 0.0734 | x | <u>0.0432</u> | 0.0287 |
| tnp_02 | 0.0681 | <u>0.0330</u> | 0.0590 | 0.0201 |
| tnp_03 | 0.0665 | 0.0283 | 0.0468 | <u>0.0383</u> |
| spms_01 | x | 0.1620 | <u>0.0686</u> | 0.0610 |
| spms_02 | x | 0.6641 | 0.0821 | <u>0.1000</u> |
| spms_03 | 19.8650 | 1.0071 | 0.0603 | <u>0.0661</u> |

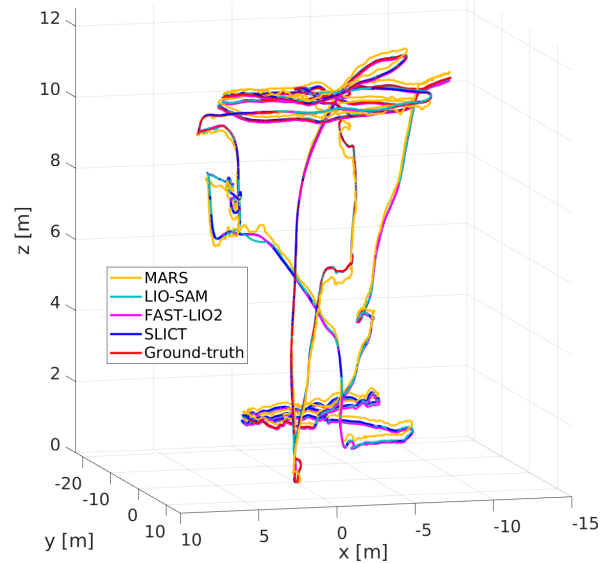


Fig. 5: Position estimates by different methods and ground truth in NTU VIRAL sequence rtp_02. SLICT and FAST-LIO2 with sub-decimeter accuracy follow the ground truth closely, while LIO-SAM and MARS have visible deviation.

Tab. I reports the result of our experiments. SLICT has the highest accuracy in the most experiments, and FAST-LIO2 has the most second best results. MARS and LIO-SAM diverge in some of the experiments. Fig. 5 shows the trajectory estimated by different methods and ground truth in sequence rtp_02.

We analyze the computational load of SLICT in the NTU VIRAL nya_02 sequence in Fig. 6. On average, it takes 165ms to complete one cycle of the algorithm (Δt_{loop} , defined as the time from one optimization operation to another), in which solving the optimization problem takes about 50ms (Δt_{solve}), and the rest is for deskew, association,

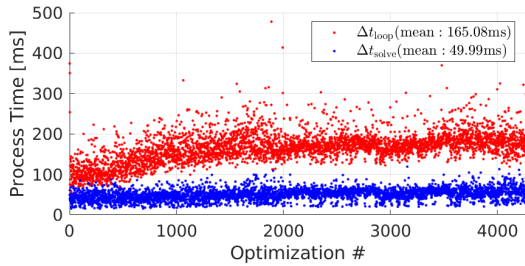


Fig. 6: Process time of SLICT in NTU VIRAL sequence nya_02.

and keyframe marginalization. Since lidar input is acquired at 100ms, currently real-time performance is not guaranteed by SLICT. Because we associate the points with surfels at five scales (from $2^1\ell$ to $2^5\ell$, where $\ell = 0.1m$), the computation load for association is at least a multitude that of direct method, which uses only one voxel scale. However, we think it is justifiable considering that SLICT gives higher accuracy, and real-time performance can be achieved by using a CPU that supports more threads.

B. Newer College Dataset

The Newer College Dataset consists of five sequences collected at New College, Oxford, featuring an Ouster lidar with 64 channels and 90-degree vertical field-of-view, and a built-in 100Hz IMU. The ground truth is obtained from ICP-based registration of lidar scan with a centimeter-resolution map captured by an imaging lidar scanner. The environment captured in the dataset features two open squares and an open park over an area of roughly $200m \times 100m$ (Fig. 8), which is several times larger than those in NTU VIRAL sequences, thus localization drift can be observed more easily.

TABLE II: ATE of SLICT and other methods on Newer College Dataset (unit [m]). The best results are in **bold**, second best are underlined. 'x' demotes a divergent experiment.

| Dataset | MARS | LIO-SAM | FAST-LIO2 | SLICT |
|-----------------------|--------|---------|---------------|---------------|
| 01_short_experiment | 2.1521 | - | 0.3883 | 0.3843 |
| 02_long_experiment | 6.0030 | - | 0.3659 | 0.3496 |
| 05_quad_with_dynamics | 0.3729 | - | 0.3443 | 0.1155 |
| 06_dynamic_spinning | x | - | 0.0800 | <u>0.0844</u> |
| 07_parkland_mound | x | - | 0.1356 | 0.1290 |

The settings are similar to that in the NTU VIRAL dataset, however for SLICT we assign 2 state estimates for each interval. This is because the dataset's main IMU, which is the built-in IMU of the Ouster lidar, has a frequency of only 100Hz. Note that LIO-SAM does not work in this case as it requires orientation estimate from the IMU.

In Tab. II, we report the ATE of the results. Again, it shows that SLICT has the best results in the most experiments, followed closely by FAST-LIO2. MARS's ATE in sequence 01, 02, 05 is similar to the reported result in [14]. As the Newer College sequences 01, 02 and 07 traverse a significantly larger area than the NTU VIRAL dataset, the

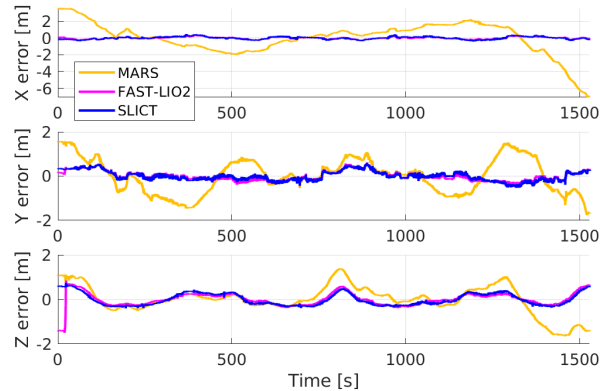


Fig. 7: Estimation error over time of the methods in the Newer College Dataset, sequence 01. We find that the error is most significant in the z direction due to the subtle changes in elevation of the area.

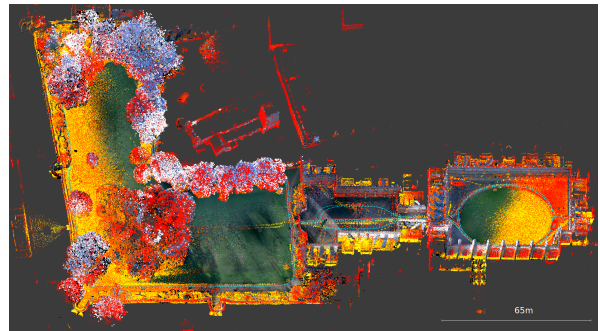


Fig. 8: The global map built by SLICT (red-to-yellow gradient based on the points' intensity) and keyframe positions (cyan dots) from sequence 02 of Newer College Dataset, superimposed on the RGB-colored prior map.

ATE increases more visibly compared to the NTU VIRAL experiments. Fig. 7 shows the localization error over time of different methods in sequence 01.

C. In-house Dataset

The in-house datasets are collected from a sensor suite consisting of an OS1-128 Lidar, an Livox Mid-70, together with a VectorNav VN100 IMU. The sensors are mounted on an All-Terrain-Vehicle (ATV) that travels around 1.5 km loop at the southern part of Nanyang Technical University (NTU) Campus (Fig. 10). This covers an area of about $400m \times 200m$, which is about four times the area of the Newer College dataset. At this scale, the effect of a loop closure module can become more appreciable, thus we add new experiments of SLICT with loop closure and pose-graph optimization functions.

The ground truth of the dataset is constructed in a similar manner to the Newer College Dataset. Specifically, we first build a static map of the environment using the survey scanner Leica RTC360 with centimeter accuracy. We then register the ouster lidar scans with this static map to obtain the ground truth pose at the lidar frequency.

Three sequences are captured. In sequence 1, we traverse

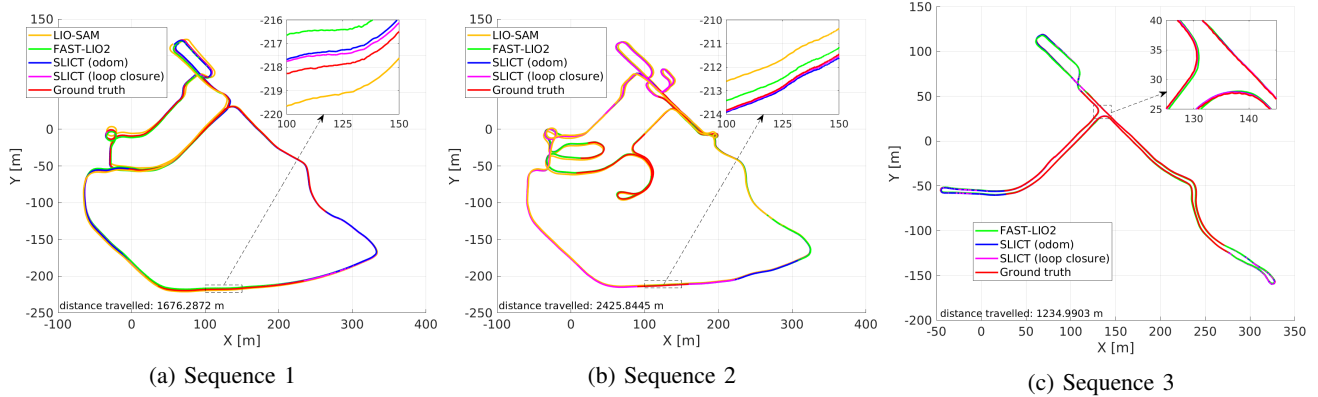


Fig. 9: Localization estimates from different methods. The zoomed-in plots show the narrow path in the dense-vegetation section (sequences 01 and 02), and the main junction (sequence 03). The elevation difference between these two points are about 13m.

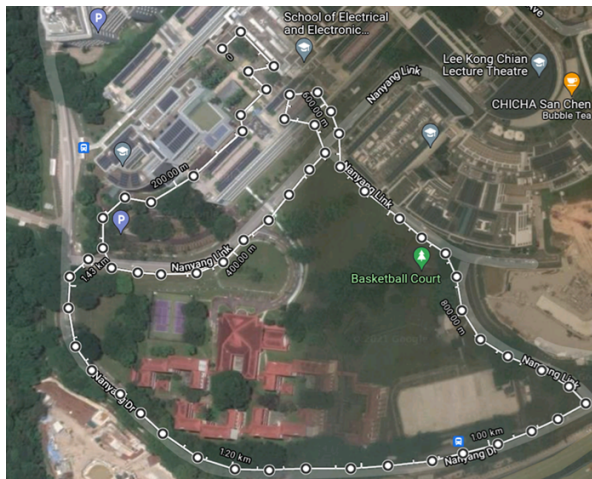


Fig. 10: Main routes in the in-house dataset.

the main routes of the environments. In sequence 2, we increase the traversed distance by revisiting some of the routes. In sequence 3, we travel back and forth on the Nanyang Link route to maximize the loop closure incidents. Fig. 9 provides an overview of the routes taken.

Similar to previous experiments, we directly merge the lidar sensors into a single input and use it for all methods. Tab. III presents the ATE of the tested methods. Due to the high-speed of the ATV (up to 30 km/h), MARS diverges in all three experiments, and LIO SAM diverges in the last experiment. Without loop closure, SLICT still has the best accuracy, and the loop closure improves the accuracy even further. We also added result of LIO-SAM with loop closure enabled to compare with SLICT.

Since the change in elevation of the environment is significant (up to 15m between the highest and lowest points) the localization error is also significant, most visibly in the z dimension (Fig. 11). Compared to the Newer College dataset in Fig. 7, we can see that the error in z direction is now almost doubled, which is the main contribution to the ATE in Tab. III. In Fig. 12, we present some views of the global

TABLE III: ATE of SLICT and other methods on in-house dataset (unit [m]). The best results are in **bold**, second best are underlined. 'x' demotes a divergent experiment. LC denotes experiments with loop-closure and pose-graph optimization.

| Dataset | MARS | LIO-SAM | FAST-LIO2 | SLICT | LIO-SAM (LC) | SLICT (LC) |
|---------|------|---------|---------------|---------------|---------------|---------------|
| seq_01 | x | 4.0784 | <u>2.0080</u> | 1.6929 | <u>1.2931</u> | 0.9815 |
| seq_02 | x | 3.7546 | <u>1.3623</u> | 1.0947 | <u>0.9685</u> | 0.7411 |
| seq_03 | x | x | <u>1.0926</u> | 0.8730 | x | 0.8577 |

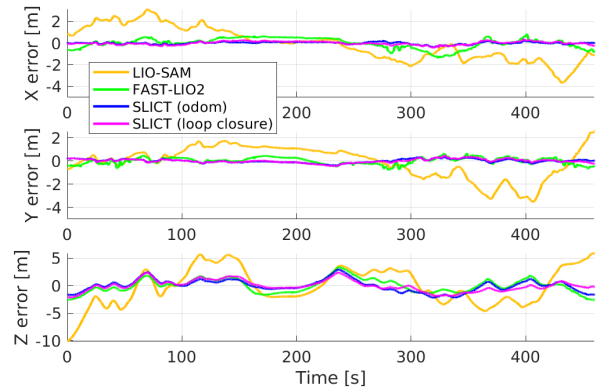


Fig. 11: Localization error in sequence 2.

map built by SLICT in sequence 2.

V. CONCLUSION

In this paper we have proposed a full-fledged multi-input Lidar-Inertial Odometry and Mapping system called SLICT. SLICT features a multi-scale global map of surfels that can be updated incrementally using the UFOMap framework. We also propose a method to associate lidar point to surfel (PTS), and a continuous-time MAP optimization of PTS and IMU-preintegration factors. We demonstrate competitive performance on public datasets even without loop closure.

To achieve a complete system, we add a simple yet effective loop closure mechanism and demonstrate its usefulness

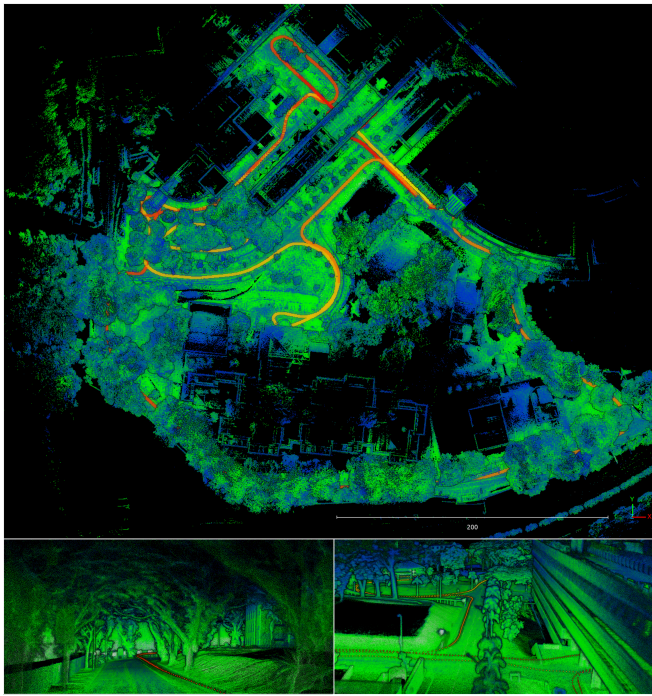


Fig. 12: The global map built by SLICT from one experiment. The two images at the bottom show the close-up views of the sections with dense vegetation and the junction areas mentioned in Fig. 9.

with our new datasets. We release the source code for the benefit of the community.

There remain many possibilities for extension of SLICT. For one, the PTS association still uses simple predicates, which can be made more efficient by some adaptive strategy. Moreover, the UFOMap framework allows one to integrate semantic information to the surfel, which has the potential to improve the association process. For the small drift, a basic loop closure mechanism sufficed, but more advanced methods can also be integrated in the future.

REFERENCES

- [1] C. Cadena, L. Carlone, H. Carrillo, Y. Latif, D. Scaramuzza, J. Neira, I. Reid, and J. J. Leonard, "Past, present, and future of simultaneous localization and mapping: Toward the robust-perception age," *IEEE Transactions on Robotics*, vol. 32, no. 6, pp. 1309–1332, 2016.
- [2] J. Zhang and S. Singh, "Loam: Lidar odometry and mapping in real-time," in *Robotics: Science and Systems*, vol. 2, no. 9, 2014.
- [3] T. Shan, B. Englot, D. Meyers, W. Wang, C. Ratti, and R. Daniela, "Lio-sam: Tightly-coupled lidar inertial odometry via smoothing and mapping," in *IEEE/RSJ International Conference on Intelligent Robots and Systems (IROS)*. IEEE, 2020, pp. 5135–5142.
- [4] T.-M. Nguyen, S. Yuan, M. Cao, Y. Lyu, T. H. Nguyen, and L. Xie, "Miliom: Tightly coupled multi-input lidar-inertia odometry and mapping," *IEEE Robotics and Automation Letters*, vol. 6, no. 3, pp. 5573–5580, May 2021.
- [5] P. Chen, W. Shi, S. Bao, M. Wang, W. Fan, and H. Xiang, "Low-drift odometry, mapping and ground segmentation using a backpack lidar system," *IEEE Robotics and Automation Letters*, 2021.
- [6] H. Wang, C. Wang, C.-L. Chen, and L. Xie, "F-loam: Fast lidar odometry and mapping," in *2021 IEEE/RSJ International Conference on Intelligent Robots and Systems (IROS)*. IEEE, 2021, pp. 4390–4396.
- [7] J. Lv, K. Hu, J. Xu, Y. Liu, X. Ma, and X. Zuo, "Clins: Continuous-time trajectory estimation for lidar-inertial system," in *2021 IEEE/RSJ International Conference on Intelligent Robots and Systems (IROS)*. IEEE, 2021, pp. 6657–6663.
- [8] W. Xu and F. Zhang, "Fast-lio: A fast, robust lidar-inertial odometry package by tightly-coupled iterated kalman filter," *IEEE Robotics and Automation Letters*, vol. 6, no. 2, pp. 3317–3324, 2021.
- [9] W. Xu, Y. Cai, D. He, J. Lin, and F. Zhang, "Fast-lio2: Fast direct lidar-inertial odometry," *IEEE Transactions on Robotics*, 2022.
- [10] J. Lin, C. Zheng, W. Xu, and F. Zhang, "R 2 live: A robust, real-time, lidar-inertial-visual tightly-coupled state estimator and mapping," *IEEE Robotics and Automation Letters*, vol. 6, no. 4, pp. 7469–7476, 2021.
- [11] J. Lin and F. Zhang, "R 3 live: A robust, real-time, rgb-colored, lidar-inertial-visual tightly-coupled state estimation and mapping package," in *2022 International Conference on Robotics and Automation (ICRA)*. IEEE, 2022, pp. 10672–10678.
- [12] D. Wisht, M. Camurri, S. Das, and M. Fallon, "Unified multi-modal landmark tracking for tightly coupled lidar-visual-inertial odometry," *IEEE Robotics and Automation Letters*, vol. 6, no. 2, pp. 1004–1011, 2021.
- [13] D. Wisht, M. Camurri, and M. Fallon, "Vilens: Visual, inertial, lidar, and leg odometry for all-terrain legged robots," *IEEE Transactions on Robotics*, 2022.
- [14] J. Quenzel and S. Behnke, "Real-time multi-adaptive-resolution-surfel 6d lidar odometry using continuous-time trajectory optimization," in *2021 IEEE/RSJ International Conference on Intelligent Robots and Systems (IROS)*. IEEE, 2021, pp. 5499–5506.
- [15] M. Bosse, R. Zlot, and P. Flick, "Zebedee: Design of a spring-mounted 3-d range sensor with application to mobile mapping," *IEEE Transactions on Robotics*, vol. 28, no. 5, pp. 1104–1119, 2012.
- [16] M. Bosse and R. Zlot, "Continuous 3d scan-matching with a spinning 2d laser," in *2009 IEEE International Conference on Robotics and Automation*. IEEE, 2009, pp. 4312–4319.
- [17] D. Duberg and P. Jensfelt, "UFOMap: An efficient probabilistic 3D mapping framework that embraces the unknown," *IEEE Robotics and Automation Letters*, vol. 5, no. 4, pp. 6411–6418, 2020.
- [18] H. Ye, Y. Chen, and M. Liu, "Tightly coupled 3d lidar inertial odometry and mapping," in *2019 International Conference on Robotics and Automation (ICRA)*. IEEE, 2019, pp. 3144–3150.
- [19] B. Welford, "Note on a method for calculating corrected sums of squares and products," *Technometrics*, vol. 4, no. 3, pp. 419–420, 1962.
- [20] T.-M. Nguyen, M. Cao, S. Yuan, Y. Lyu, T. H. Nguyen, and L. Xie, "Viral-fusion: A visual-inertial-ranging-lidar sensor fusion approach," *IEEE Transactions on Robotics*, vol. 38, no. 2, pp. 958–977, 2022.
- [21] S. Agarwal and K. Mierle, "Ceres solver: Tutorial & reference." [Online]. Available: <http://ceres-solver.org/>
- [22] T.-M. Nguyen, S. Yuan, M. Cao, Y. Lyu, T. H. Nguyen, and L. Xie, "Ntu viral: A visual-inertial-ranging-lidar dataset, from an aerial vehicle viewpoint," *The International Journal of Robotics Research*, vol. 41, no. 3, pp. 270–280, 2022.
- [23] M. Ramezani, Y. Wang, M. Camurri, D. Wisht, M. Mattamala, and M. Fallon, "The newer college dataset: Handheld lidar, inertial and vision with ground truth," in *2020 IEEE/RSJ International Conference on Intelligent Robots and Systems (IROS)*, 2020, pp. 4353–4360.
- [24] F. Dellaert, R. Roberts, V. Agrawal, A. Cunningham, C. Beall, D.-N. Ta, F. Jiang, lucacarlone, nikai, J. L. Blanco-Claraco, S. Williams, ydjian, J. Lambert, A. Melim, Z. Lv, A. Krishnan, J. Dong, G. Chen, K. Chande, balderdash devil, DiffDecisionTrees, S. An, mpaluri, E. P. Mendes, M. Bosse, A. Patel, A. Baid, P. Furgale, matthewbroadwaynavenio, and roderick koehle, "borglab/gtsam." May 2022. [Online]. Available: <https://doi.org/10.5281/zenodo.5794541>